

Resolution and Reciprocity in Microspherical Nanoscopy: Point-Spread Function Versus Photonic Nanojets

A.V. Maslov^{1,*} and V.N. Astratov^{2,†}

¹*University of Nizhny Novgorod, Nizhny Novgorod, 603950, Russia*

²*Department of Physics and Optical Science, Center for Optoelectronics and Optical Communication, University of North Carolina at Charlotte, Charlotte, North Carolina 28223-0001, USA*

 (Received 29 September 2018; revised manuscript received 17 March 2019; published 3 June 2019)

This paper pertains to a long-standing debate about the quantification criteria and mechanisms of optical superresolution in microsphere-based nanoscopy. Its super resolution capability has been closely linked in the literature to the width of photonic nanojets. A comprehensive and systematic comparison of the resolution obtained from the point-spread function (PSF) and the nanojet width is provided here. In both cases, the Maxwell equations are rigorously solved in a two-dimensional geometry using similar microsphere parameters. By carrying out the analysis in a rather broad range of parameters (microsphere size, object-to-microsphere separation), the assumption that the standard resolution defined by the PSF can be deduced from the nanojet focusing properties is disproved. The resolution values that result from the PSF and magnification are studied in two regimes: with and without the excitation of whispering-gallery-mode resonances in the microparticle. Unlike previous studies of nanojet focusing, the presented results summarize the true resolution capability of microspheres stemming from the classical point-emission geometry. It is also argued that a higher resolution capability can result from the coherence of illumination or the resonantly increased role of near fields in nanoplasmonic arrays.

DOI: [10.1103/PhysRevApplied.11.064004](https://doi.org/10.1103/PhysRevApplied.11.064004)

I. INTRODUCTION

Microspherical nanoscopy emerged in 2011 as an extraordinarily simple technique allowing imaging of dielectric and metallic nanostructures with a resolution that significantly exceeds the classical diffraction limit [1]. In this method, a dielectric microsphere creates a magnified virtual image of an object placed in contact with it, as schematically illustrated in Fig. 1. The upper limit of the diffraction-limited resolution of such a contact microlens can be estimated based on the solid-immersion lens (SIL) concept as $\lambda/(2NA)$, where the numerical aperture $NA = n_s \sin \theta$ is defined by the object-space (or, here, the microsphere) index n_s and the collection angle θ [2–4]. Shortly after, the use of high-index ($n_s \gtrsim 1.8$) microspheres [5], which are fully liquid-immersed [6–8] or embedded in elastomeric slabs [9–12], was proposed. The liquid immersion made possible the imaging of cells, subcellular structures, and proteins [13–16]. Based on the SIL concept, it allowed the object-space index to be increased up to $n_s \sim 2$, which limits the far-field resolution at approximately $\lambda/4$. Liquid-immersed or embedded high-index microspheres can be micromanipulated by a variety of

techniques [17–20], allowing large areas of the samples to be scanned. Stitching of the images can result in the development of a new generation of ultra-high-resolution fast-scanning optical microscopes [18].

The significant interest to the field of microspherical nanoscopy is driven by two factors. First, the method is so simple that it can find broad applications for imaging subcellular structures, proteins, biological molecules, plasmonic nanoparticles, or integrated circuits and it does not necessarily require fluorescent (FL) labeling. Second, this method can result in resolution values which are higher than the diffraction limit. The fundamental reason for its superresolution capability is of current interest [21–26].

The experimental resolution depends on many factors: (a) the type of object—near fields can be resonantly enhanced in nanoplasmonic structures; (b) the refractive indexes of the microlens and the surrounding medium—the optimal index contrast for virtual imaging is within the 1.3–1.7 range, but higher average indexes of the microsphere-medium system can facilitate higher resolution; and (c) the type of illumination—confocal illumination can provide a better signal-to-noise ratio compared to wide-field illumination (it can also provide better resolution by using extremely narrow pinholes—however, it is rather difficult to realize this resolution enhancement in the case of weak signals [11]). The excitation of Mie

*avmaslov@rf.unn.ru

†astratov@uncc.edu

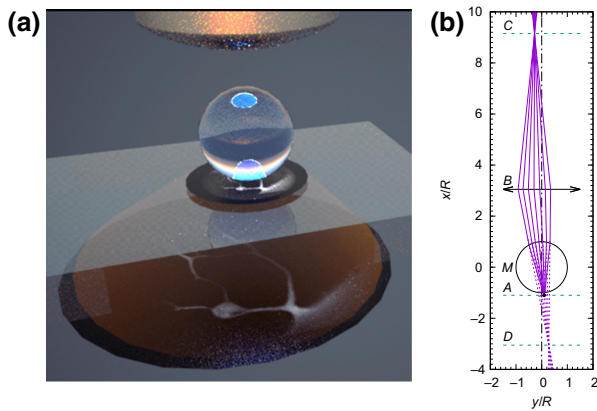


FIG. 1. (a) Imaging of a biomedical sample through a contact microsphere. (b) Geometric ray tracing and virtual image formation. A point source located in the object plane A and displaced from the optical axis emits light that is collected by the microsphere M and redirected to the microscope objective B . A sharp image will be formed in the detector plane C when the plane of focus for the system of the lens B and the detector C coincides with the plane D of the virtual image formed by the microsphere. If the microscope objective is modeled as a single lens (as drawn here), the unmagnified virtual image is projected on the detector when the distances from B to D and from C to B are twice the focal distance of the lens.

resonances in microspheres and the use of oblique or coherent illumination can favor higher resolution. Since in different experimental studies these conditions and parameters have varied greatly, it is rather problematic to present a coherent picture of the developments in this area. We summarize some of the existing experimental results on microspherical nanoscopy in Table I. The table contains information about the imaged objects, the size and material of the microspheres, the refractive indexes of the microspheres and the surrounding media, the type of illumination, and the resultant resolution.

The main conclusion of Table I is that microspherical nanoscopy provides an extremely simple and versatile method of imaging that works in a similar way to SIL, but with somewhat higher resolution. The initial experiments were interpreted using semiquantitative resolution criteria based on the discernibility of small features and that gave rise to resolution claims of about $\lambda/8$ – $\lambda/14$ [1] or even $\lambda/17$ [27]. More rigorous resolution quantifications based on the convolution of the object shape with the point-spread function (PSF) [8,10–12] led to somewhat reduced resolution values of approximately $\lambda/6$ – $\lambda/7$, which still far exceed the classical diffraction limit determined by the microscope objective and, most interestingly, even the SIL limit determined by the high-index microspheres. Microspheres provide good near-field coupling conditions with nanoscale objects (gaps below $\lambda/2$) due to small size of the contact area. The drawback, however, is that the field of view is limited by about a quarter of the sphere diameter

[6]. It has been demonstrated that the field of view can be increased by translating the microspheres by a variety of techniques [10,17–20,30] followed by stitching of the corresponding images.

The theoretical explanation of superresolution initially proposed in Ref. [1] was based on a notion that focusing and imaging are fundamentally related by the reciprocity principle [31,32]. This implies that subwavelength focusing by microspheres directly translates into the subwavelength PSF width, which defines the resolution. While such a direct relation has not been demonstrated, many theoretical studies have been dominated by this notion and multiple research groups have performed simulations of nanojets in lieu of imaging (see, e.g., Refs. [28,33–43]). Although this seems to be intuitively appealing, the direct application of reciprocity to the focusing regime does not make it a point-source emission regime, as required for resolution quantification according to the classical definitions [44,45]. Indeed, let us take the case of plane-wave focusing. The initial plane wave produces scattered waves that propagate in all possible directions and can also form a nanojet. Furthermore, the scattering generates evanescent fields that decay from the surface and can also contribute to the nanojet [46–50]. The reciprocity principle says that the conjugate of the focusing solution will also be a solution of the Maxwell equations [51]. This conjugation means that the scattered waves become incident on the particle and produce the backwardly propagating plane wave. The conjugation does not change the direction of evanescent decay—the fields still decay from the particle surface. It is apparent that the reciprocal field distribution does not correspond to the emission of a point source. Thus, making the conjugation of the focusing regime does not give us direct information about the point-source emission regime that defines the PSF [44,45]. While this direct conjugation is apparently not very useful, focusing and emission do have similarities. If focusing produces a nanojet with some subwavelength features, this implies that if we put a point source at that location, its high spatial-frequency Fourier components will produce outgoing radiation. We can anticipate that the emission of such current components can potentially form a sharper image and, thus, enhance resolution. However, the image formation involves not only the presence of high spatial-frequency components but also their superposition, which can only be accounted for by solving the point-source emission problem.

Another drawback of attributing superresolution to nanojets is that the width of photonic nanojets can be only fractionally smaller than the diffraction limit in air (approximately $\lambda/2$) and only under a special choice of parameters for the microspheres [46–49]. The jet width is smallest at approximately $\lambda/3$ for 2–3 μm particles; for particles larger than 5–6 μm , the width exceeds $\lambda/2$ [50]. In contrast, the experimentally reported resolution reaches approximately $\lambda/6$ – $\lambda/7$. For these reasons, we

TABLE I. Summary of resolution quantification at different experimental conditions of microsphere-based imaging. The resolution estimates are based on experimentally discernable minimal feature sizes or on more rigorous procedure of convolution with one-dimensional (1D) and, especially, with two-dimensional (2D) PSFs. Notation: MRF, minimally resolved features; BTG, barium titanate glass; IPA, isopropyl alcohol; PDMS, polydimethylsiloxane; BRD, Blu-ray disk; CPU, central processing unit; LPSIM, localized plasmonic structured illumination microscopy; CLSM, confocal laser scanning microscopy; PIP, postimaging processing.

Reference	Object	MS material– background, size	Illumination	Modality	Estimated resolution
Wang <i>et al.</i> [1]	Gratings, plasmonic structures, BRD	SiO ₂ -air, $D \sim 5 \mu\text{m}$	White-light, 400–750 nm	Wide-field; transmission, reflection	$\lambda/8 - \lambda/14$ (MRF)
Darafsheh <i>et al.</i> [6]	Plasmonic dimers, BRD	BTG-IPA, $D \sim 2-220 \mu\text{m}$	White-light, 400–750 nm	Wide-field; reflection	$\lambda/7 - \lambda/4.5$ (MRF)
Li <i>et al.</i> [13]	Adenovirus, BRD, nanopores	BTG-H ₂ O, $D \sim 100 \mu\text{m}$	White-light, 390–700 nm	Wide-field; reflection	$\lambda/6$ (MRF)
Yang <i>et al.</i> [14]	FL labeled, nanospheres, subcellular structures	BTG-H ₂ O, $D \sim 60 \mu\text{m}$	FL, 680 nm	FL imaging	$\lambda/7$ (MRF)
Krivitsky <i>et al.</i> [17]	Plasmonic dimers, grating	SiO ₂ -air, $D \sim 7 \mu\text{m}$	White-light, 400–750 nm	Scanning-wide- field; reflection	$\lambda/10 - \lambda/17$ (MRF)
Darafsheh <i>et al.</i> [7]	Plasmonic dimers	BTG-IPA, $D \sim 10-53 \mu\text{m}$	Narrow-band, 405 nm	CLSM	$\lambda/6$ (1D convolution)
Yan <i>et al.</i> [27]	Plasmonic nanoholes, nanowires	Fused SiO ₂ -air, $D = 2.5-7.5 \mu\text{m}$	Narrow-band, 408 nm	CLSM	$\lambda/17$ (MRF)
Allen <i>et al.</i> [10]	Plasmonic dimers	BTG-PDMS, $D \sim 5-53 \mu\text{m}$	Narrow-band, 405 nm	CLSM	$\lambda/6 - \lambda/7$ (2D convolution)
Allen <i>et al.</i> [8]	Plasmonic dimers	BTG-IPA, $D \sim 8-10 \mu\text{m}$	Narrow-band, 405 nm	CLSM	$\lambda/6.6 - \lambda/7.3$ (2D convolution)
Wang <i>et al.</i> [18]	BRD, CPU, nanowires, FL cells	BTG-H ₂ O, $D \sim 27-70 \mu\text{m}$	White-light, centered at 550 nm	Scanning-wide- field; reflection	$\lambda/6.3 - \lambda/8.4$ (2D convolution)
Yang <i>et al.</i> [28]	Silicon grating	BTG-H ₂ O, $D \sim 3-21 \mu\text{m}$	White-light, 400–700 nm	Wide-field; reflection	$\lambda/4 - \lambda/7$ (1D convolution)
Astratov <i>et al.</i> [16], Brettin <i>et al.</i> [58]	FL labeled proteins or nanospheres	BTG-plastic, $D \sim 8-20 \mu\text{m}$	FL, 604–644 nm (proteins), 505–555 nm (nanospheres)	Wide-field FL; coupling with plasmonic metasurface	$\lambda/7$ (2D convolution)
Bezryadina <i>et al.</i> [29]	FL labeled nanospheres	TiO ₂ -H ₂ O $D \sim 20 \mu\text{m}$	FL, approximately 570 nm	Wide-field FL; LPSIM, with PIP	$\lambda/10$, (2D convolution)

suggest in this work that the capability of microspheres to form photonic nanojets does not adequately explain their super resolving power—or, at least, this analogy should be exercised extremely carefully, with the full understanding that the calculations of nanojets cannot be directly applicable to explaining the experimentally observed resolution. Sometimes, the superresolution is attributed directly to the subwavelength size of the excitation volume generated on the shadow side of the microsphere by the nanojets [52]. The photonic nanojet can be more suitable for understanding resolution in confocal microscopy, but it seems to be less relevant to wide-field microscopy, where most of the experimental results have been obtained.

It should also be noted that the calculation of photonic nanojets is a relatively straightforward task, implemented in many commercial software packages for electromagnetic modeling, whereas the finding of images based on a rigorous solution of the Maxwell equations typically requires a special treatment. The relative simplicity of the nanojet calculation, in contrast to the significantly more complex microsphere-based imaging, has stimulated a somewhat simplified approach to imaging based on substituting true imaging modeling with that of nanojets and claiming a strong connection between the focusing and superresolution [28,33–43].

To shed light on the relevance of photonic nanojets for defining the resolution, in this work we compare the imaging and focusing properties of dielectric microspheres based on exact numerical solutions of the Maxwell equations. Our imaging results are obtained for a point source emitting near a microsphere, in the spirit of classical resolution theory [44,45]. To simplify the analytical and numerical calculations, we adopt a two-dimensional (2D) model that should correctly reproduce the electromagnetic process of image formation, including various near-to-far-field transformations that may exist for subwavelength source-to-microsphere distances. Previously, a 2D model of photonic nanojets has been shown to capture all the essential features of a more complete three-dimensional (3D) model [53]. Besides microspheres, microcylindrical lenses are also used in experiments [8,54]. Our 2D calculations are not a replacement for the full 3D modeling required for accurate fitting of the experimental imaging results obtained using microspheres but, rather, an attempt to provide a physical insight into the main effects and to explain the main dependencies of such imaging. One of the possibilities for conducting full 3D modeling is to use some existing software based, for example, on the finite-difference time-domain (FDTD) method [55]. However, it is an extremely extensive computational task to complete an analysis comparable to this work for a 3D case. Despite the simplification in the geometry, our approach provides very accurate descriptions of all of the electromagnetic properties, in particular, when operating at resonance with whispering gallery modes (WGMs), whereas FDTD approaches can sometimes provide less reliable results [56] or, at least, require longer computational times and larger resources in order to obtain sufficiently accurate results.

All of the factors that can additionally enhance the resolution in the experimental situation—for example, plasmonic enhancements of near fields in nanostructured metallic objects [16,57,59] or plasmonic structured illumination [29,60]—are outside the scope of this work. We also do not consider the imaging of extended sources or several point sources oscillating with specific phases, which can provide possibilities for coherent imaging with infinite resolution [25,60].

We calculate images as they would be seen in an optical microscope with the objective lens focused at different depths, i.e., planes of focus. Here the term "plane of focus" indicates the plane at which an object should be located to provide the sharpest image. The plane of focus depends on the parameters of the imaging system [the lens and the detector in Fig. 1(b)] and, in general, differs from the focal plane of the lens alone. We show that these images are dramatically different from the distributions of the electromagnetic field. The imaging for arbitrary gaps between point sources and microspheres is analyzed. Images of point sources just outside of the microspheres (zero gap) were considered previously by

solving the Maxwell equations using the finite-element [22] and expansion [21] methods. The gap significantly affects imaging through magnification, which is also analyzed. Our results show that the evaluation of resolution in microspherical nanoscopy requires rigorous solutions of the Maxwell equation for point sources and that the calculations of photonic nanojets generally cannot be used for this purpose.

II. FORMULATION OF THE PROBLEM

The studied physical model is illustrated in Fig. 2. Two specific cases are considered. In the first case, shown in Fig. 2(a), a particle focuses an incident plane wave. In the second case, shown in Fig. 2(b), a point source of current emits near a particle. The emitted radiation is collected by a lens, which forms an image on a detector. Both cases are considered in the 2D geometry, in which there is no dependence on the z coordinate. The polarization is transverse magnetic (TM), i.e., the field components are E_x , E_y , and H_z . The parameters are as follows: R is the radius of the particle and n_s is its refractive index, n_b is the index of the background space, d is the distance from the particle surface to the current location, and ω is the operating frequency. The current density has the following form:

$$\mathbf{J}(x,y) = j_0 \hat{y} \delta(x+R+d) \delta(y). \quad (1)$$

Our results below are obtained at $n_b = 1$ for the background and at $n_s = 1.4$ for the microparticle. In practice, however, a liquid environment and high-index microspheres are often used [6–8]. The imaging properties in this case can be deduced directly from the $n_b = 1$ case.

Indeed, let us assume that a point source $\mathbf{j}_0 \delta(x) \delta(y)$ emits in a medium with some arbitrary distribution of refractive index $n_1(x,y)$. We assume that this point source produces fields $\mathbf{E}_1(x,y)$ and $\mathbf{H}_1(x,y)$. If we increase the refractive index everywhere by a factor of m and simultaneously reduce all size parameters by the same factor, the

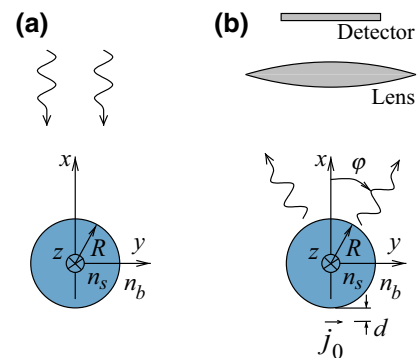


FIG. 2. The geometry of the problem. (a) The focusing of a plane wave by a particle. (b) The imaging of a point source emitting near a particle.

new index distribution becomes $n_2(x, y) = mn_1(mx, my)$. From the Maxwell equations, we obtain that the fields generated by the same point source can be directly expressed in terms of the known field distributions as $\mathbf{E}_2(x, y) = \mathbf{E}_1(mx, my)$ and $\mathbf{H}_2(x, y) = \mathbf{H}_1(mx, my)$. Since the image depends on the relative field strength, the only effect of the uniform increase of the index and the size compression is the overall increase of the resolution by m . Thus, our simulations are directly relevant to the case of imaging inside a background material as long as the index contrast remains at $n_s/n_b = 1.4$.

This situation shows that imaging by liquid-immersed or plastic-embedded high-index ($n_s \sim 2$) barium titanate glass (BTG) microspheres [6–16, 18] should provide higher resolution compared to silica ($n_s = 1.46$) spheres in air [1, 17]. The resolution advantage of BTG spheres needs to be estimated for each material combination, but in general it is close to 1.4.

III. CALCULATION OF FIELDS AND IMAGES

The circular geometry of the particle makes it natural to use analytical methods of expanding the fields into angular series. The time dependence of all fields is $e^{-i\omega t}$. In the TM case, it is convenient to solve the problem for the transverse magnetic component $H_z(x, y)$.

To find the scattered fields in the case shown in Fig. 2(a), we expand the fields inside and outside the cylinder as well as the incident wave. Matching the fields at the $\rho = R$ boundary, we obtain the standard expressions for the expansion coefficients (see, e.g., Ref. [61]).

The solution for the case shown in Fig. 2(b) proceeds in the same manner, the point current given in Eq. (1) and the fields generated by it being expanded into a series. After the fields are calculated, we can find the field in the far-field region:

$$H_z(x, y) = \frac{f(\varphi)}{\sqrt{k_b \rho}} e^{ik_b \rho - i\pi/4}, \quad (2)$$

where $k_b = n_b k$ and $k = \omega/c$. The angular distribution function $f(\varphi)$ is obtained from the expansion. The far field can also be represented as follows:

$$H_z(x, y) = \int_{|g| < k_b} dg e^{ihx + igy} \tilde{H}_z(g), \quad (3)$$

where $\tilde{H}_z(g)$ is the Fourier component and $g^2 + h^2 = k_b^2$. Evaluating the integral in Eq. (3) asymptotically at $\rho \rightarrow \infty$ and comparing with Eq. (2) gives us the Fourier component:

$$\tilde{H}_z(g) = \frac{f(\varphi)}{\sqrt{2\pi} k_b \cos \varphi}, \quad g = k_b \sin \varphi. \quad (4)$$

An objective lens collects the far field and forms an image on the detector. For an ideal objective lens with NA = 1

and without magnification, the image is equivalent to the intensity distribution of the back-propagated far field in the plane of focus (defined by x). The knowledge of \tilde{H}_z allows us to formally back-propagate the field to any point in space and find the image intensity:

$$I(x, y) = |H_z(x, y)|^2. \quad (5)$$

The back-propagated field at some location differs from the true field there since this procedure is equivalent to image formation and is not a solution of an inverse scattering problem [62]. If the far field is generated by some sources in free space, the sharpest image is observed when the plane of focus passes through the sources. Thus, by scanning over various positions x of the plane of focus, we search for the location of the far-field sources. Generally, such scanning mimics finding the sharpest image in experimental microscopy. Any magnification of the objective lens only scales the image on the detector, i.e., along y .

IV. POINT-SOURCE EMISSION AND IMAGING IN FREE SPACE

The emission of a point source in free space is an analytically solvable problem that can be used for verification. The field created by point source $j_0 \hat{y} \delta(x) \delta(y)$ is

$$H_z(x, y) = -H_0 i \pi n_b H_1^{(1)}(k_b \rho) \cos \varphi, \quad (6)$$

where $H_1^{(1)}$ is the Hankel function of the first kind and the constant $H_0 = j_0 \omega / c^2$ is a magnetic amplitude. For $n_b = 1$, we obtain $|H_z(x, y = 0) / H_0| = 1$ at distance $k\rho \approx 6.3405$ or $\rho/\lambda \approx 1.0091$ from the source. There is no radiation emitted in the direction of the current source, i.e., along the y axis. The magnetic field $H_z(x, y)$ diverges as $\rho \rightarrow 0$. One can calculate the far field and then back-propagate it to find the intensity distribution at an arbitrary plane of focus. The back-propagated field at $x = 0$ becomes

$$H_z(x = 0, y) = -H_0 2n_b \frac{\sin(k_b y)}{k_b y}. \quad (7)$$

It is convenient to introduce a unitless image intensity:

$$\mathcal{I}(x, y) = \left| \frac{H_z(x, y)}{H_0} \right|^2. \quad (8)$$

For the point source, we obtain

$$\mathcal{I}(x = 0, y) = 4n_b^2 \left(\frac{\sin(k_b y)}{k_b y} \right)^2. \quad (9)$$

Unlike the field intensity, which diverges at $\rho = 0$, the created image $\mathcal{I}(x = 0, y)$ always has a finite value. Equation (9) is an exact solution of the Maxwell equations in the 2D case and does not rely on the paraxial approximation.

V. SCATTERING CROSS SECTION, EMITTED POWER, AND RESONANCES

We start by studying the optical properties of the particle that affect image formation. Figure 3(a) shows the scattering cross section when the particle is illuminated by a TM-polarized plane wave. It shows large-scale oscillations and small narrow peaks. The large-scale oscillations are related to the interference of the light passed through the particle and through the background and have a period of $kR \approx \pi/(n_s - n_b) \approx 7.9$. The small narrow peaks are signatures of various resonances excited in the particle. The properties of some of these resonances are summarized in Table II. Despite their significant Q factors, the resonances are barely seen in the scattering cross section because of the weak coupling to the incident plane wave. The resonance should be more visible if the excitation source is put near to the particle surface.

Figure 3(b) shows the spectrum of the power emitted by the point source located near the particle. One can see a comb of resonant peaks with much higher peak-to-background ratios at sufficiently large values of kR but at the same positions as in Fig. 3(a). Their amplitudes grow rapidly with kR . The strong enhancement is related to the resonances with the lowest radial number. The field of these modes does not have nodes inside the particle and decays outside. Figure 4(a) shows the dependence of the emitted power on the distance kd to the particle. On resonance ($kR = 20.382, 23.476$), the power decreases with distance for small kd and then starts to oscillate weakly. Off

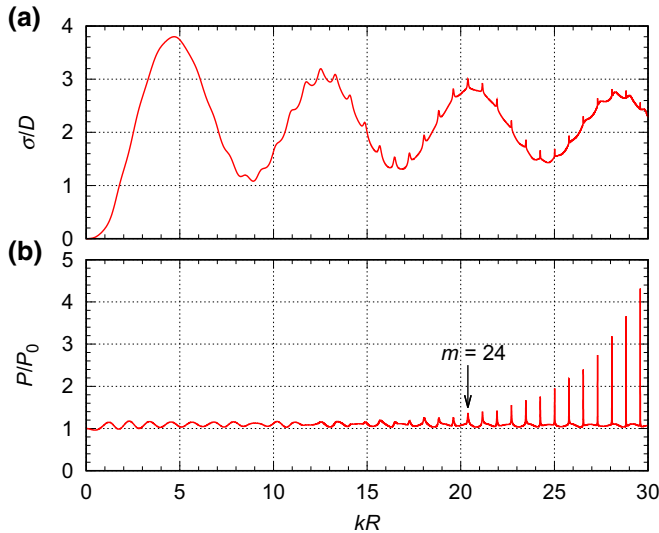


FIG. 3. (a) The scattering cross section σ (normalized to the geometric cross section $D = 2R$) for a cylinder with $n_s = 1.4$ as a function of kR . (b) The power P emitted by a point source (normalized to the free-space emission P_0) located at a distance $kd = 1$ from the cylinder surface. The WGM resonance with the azimuthal number $m = 24$ is labeled in panel (b) as a reference.

TABLE II. The properties of several TM resonances for $n_s = 1.4$ and $n_b = 1$: azimuthal numbers m , resonant frequencies kR , D/λ , and Q factors.

m	kR	D/λ	$\log_{10}(Q)$
23	19.602	6.2395	2.36
24	20.382	6.4878	2.47
25	21.158	6.7348	2.59
28	23.476	7.4726	2.92
34	28.0675	8.93416	3.59

resonance, the power shows only some rather weak oscillations with distance. The strong enhancement of the power emission for sources near the particle suggests that the resonances can significantly impact the image formation.

The power is emitted at all possible angles and can be represented as follows:

$$P = \int_0^{2\pi} d\varphi p(\varphi), \quad (10)$$

where $p(\varphi)$ is the angular power density. Without the microparticle, the power distribution is $p(\varphi) \propto \cos^2 \varphi$, which can be obtained directly from Eq. (6). Typical distributions of $p(\varphi)$ are shown in Fig. 4(b). In the nonresonant case, $kR = 20$, the emission into the upper half space has a narrower angular width and higher intensity as compared to that into the lower half space. Due to rather narrow angular emission even lenses with NA ~ 0.5 can be used without loss of resolution. In the case of resonances, $kR = 20.382, 23.476$, multiple interference peaks can be observed.

Thus, the focusing of plane waves and the imaging of point sources are quite different because of the coupling

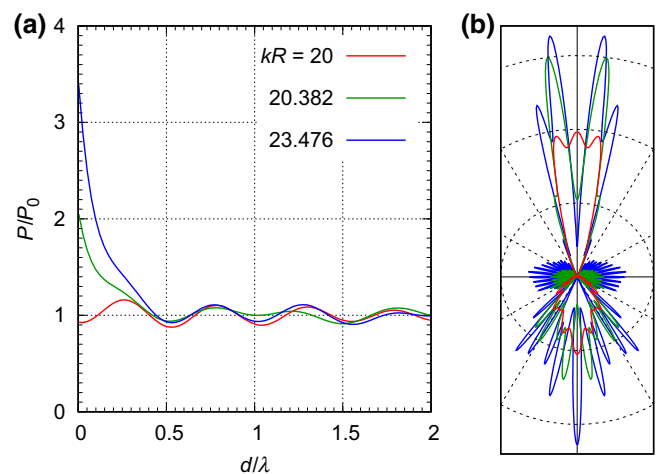


FIG. 4. (a) The normalized power P/P_0 emitted by a point source as a function of the gap $d/\lambda = kd/(2\pi)$ for various values of kR . (b) The angular distribution of the emitted power $p(\varphi)$ for the same kR as in panel (a) at $kd = 1$.

strength to the microsphere WGM resonances. The coupling of incident plane waves to WGM resonances is so weak that the corresponding peaks in the scattering cross section are hardly visible. In contrast, the coupling of point sources located in the near-field proximity to microspheres is so strong that it greatly modifies the emission spectra, leading to an almost full redistribution of the emitted power into the WGMs for large kR . This means that, in practice, the imaging of fluorescent species, such as dyed nanoparticles or biomedical structures, is likely to take place in the resonant regime irrespective of the characteristics of the point sources or microspheres. This has important consequences for the resolution of the system, since resonant imaging may have higher resolution due to the resonant enhancement of the evanescent fields at the WGM frequencies [26].

VI. FOCUSING OF PLANE WAVES AND PHOTONIC NANOJETS

The focusing of an incident plane wave is illustrated in Fig. 5, which shows field distributions for particles with several sizes kR . If the operating wavelength is $\lambda = 650$ nm, the value $kR = 10$ corresponds to the particle diameter $D = 2R = 2.069 \mu\text{m}$ and $kR = 30$ to $D = 6.207 \mu\text{m}$. For the small nonresonant particle ($kR = 10$), the formation of a photonic nanojet can be observed just at the surface of the particle. As the size kR becomes larger, the nanojet peak moves away from the surface. The presence of resonances does not change the formation of the nanojet

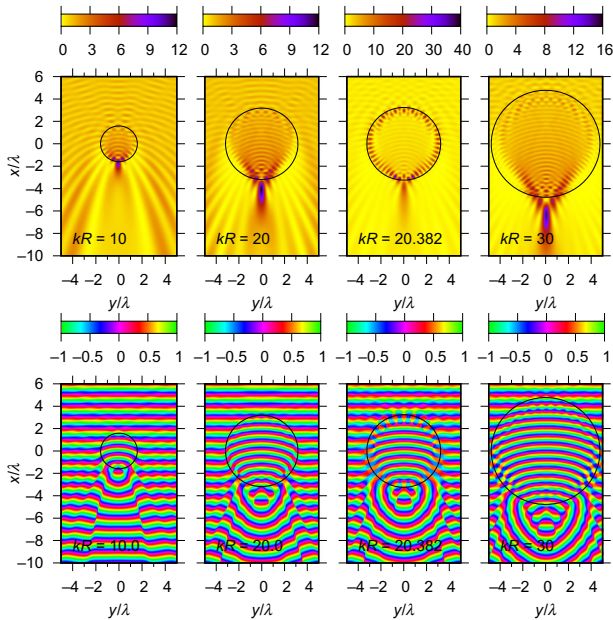


FIG. 5. Top panels: the intensity distribution $|H_z/H_0|^2$ created by a plane wave incident on a particle with $n_s = 1.4$ for several values of kR . Bottom panels: the phase distribution φ/π for the same parameters.

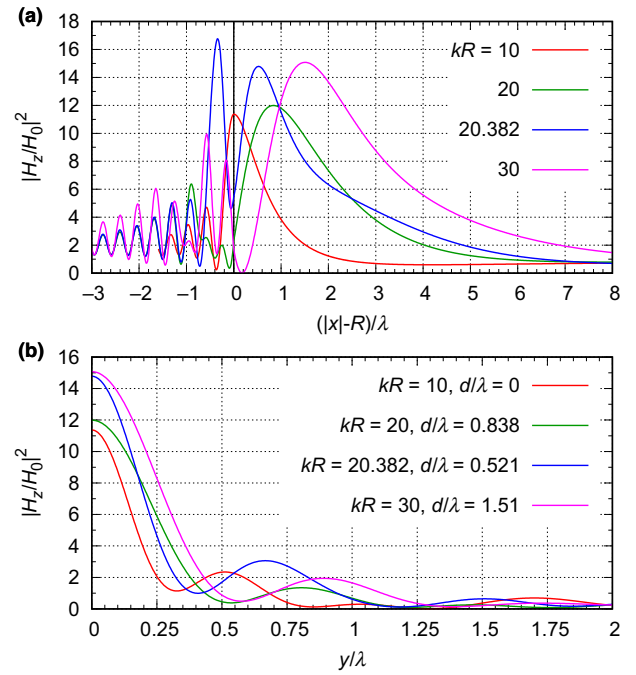


FIG. 6. (a) The intensity distribution for photonic nanojets along the x direction (along the direction of plane-wave incidence) as a function of the distance $d = |x| - R$ to the particle surface. The vertical solid line at $d = 0$ shows the particle boundary. (b) The intensity distribution along the y direction at the maximum of the x distribution.

qualitatively. However, the intensity of the excited resonance can significantly exceed the maximum intensity of the nanojet.

To study the photonic nanojets more quantitatively, Fig. 6 displays the profiles of the field distributions shown in Fig. 5. Figure 6(a) shows the field distributions along x at $y = 0$ as a function of the distance from the surface $d = |x| - R$. As the size increases from $kR = 10$ to $kR = 30$, the peak moves from the particle surface and its magnitude increases. The presence of resonances (compare the cases $kR = 20$ and $kR = 20.382$) slightly increases the maximum value and displaces the maximum closer to the surface. The intensity approaches $|H_z/H_0|^2 \rightarrow 1$ far away from the particle at $d/\lambda \gg 1$.

Figure 6(b) shows the normalized intensity $|H_z/H_0|^2$ of the nanojets in the transverse direction at the x positions that correspond to the maxima in Fig. 6(a). The intensity is a maximum on the axis $y = 0$. Far away from the axis at $y/\lambda \gg 1$ [outside of the range of Fig. 6(b)], $|H_z/H_0|^2 \rightarrow 1$. Following the common approach [46–49], we characterize the focusing by using the full width at half maximum (FWHM) of the central peak. The smallest width 0.32λ is observed for the nanojet formed by the smallest particle, $kR = 10$. This width is approximately equal to $0.5\lambda/n_s$ [63]. For the $kR = 20$ particle, the width is 0.49λ and for $kR = 30$ the width is 0.54λ .

In the resonant case $kR = 20.382$, the width is 0.39λ . Apparently, the smallest width is obtained when the evanescent waves contribute to nanojets with maxima at or very near the surface, as for $kR = 10$.

A potential resource for increasing the resolution in experimental situations is related to the possibility of the partial contribution of coherent illumination [44,45]. It can be realized if a wavefront with an abrupt phase change of π is used to illuminate two point objects (two closely spaced nanospheres, nanoplasmonic dimers, etc.). By adjusting the illumination conditions it should be possible to excite the point objects by out-of-phase parts of the wavefront. The coherent emission of the out-of-phase point sources should result in the visibility of the zero-intensity midpoint for any, even infinitely small, separation between them [25,60,64]. The rapid phase variations near the nanojets can also be attributed to the Gouy anomaly. Figure 5 (bottom) shows the phase distributions created by the plane wave. It is seen that the rapid variations of the phase indeed take place along the illumination wavefront, in proximity to the microsphere. It should be noted, however, that such variation of the phase takes place away from the anticipated contact point with the structure (from the vertical axis of the microsphere). Through the use of oblique illumination, the position of abrupt variation of the phase can be shifted toward the vertical axis. This can be an important factor in providing a possible explanation of recent observations of better resolution at oblique illumination of microspheres [18].

VII. POINT-SPREAD FUNCTION AND RESOLUTION

One of the key characteristics of an imaging system is its PSF, i.e., the image created by a point source [44,45]. Let us first discuss the PSF for a point source [see Eq. (1)] emitting in free space. To model free space, we simply take a very small index contrast of the particle (see Fig. 7). It is seen that the images are different from the intensity distributions. While the intensity diverges at the particle location [see Eq. (6)], the image does not. Also, there is no emission at the source plane $x = -R - d$, since the current does not emit along its direction. The image, however, has a finite intensity in that plane.

Figure 7(c) shows the image intensity in the transverse direction. Let \mathcal{W} denote the FWHM of the image. From Fig. 7(c), we obtain $\mathcal{W}/\lambda = 0.447$. This value is the free-space resolution according to the Houston criterion [45,65]. If we use the first zero of the image, the Rayleigh criterion [45,66], we obtain 0.5, which is a similar value. The image along y and the actual field intensity are shown in Fig. 7(d). The image width in the axial x direction is about 1.25λ , which is significantly larger than the transverse width.

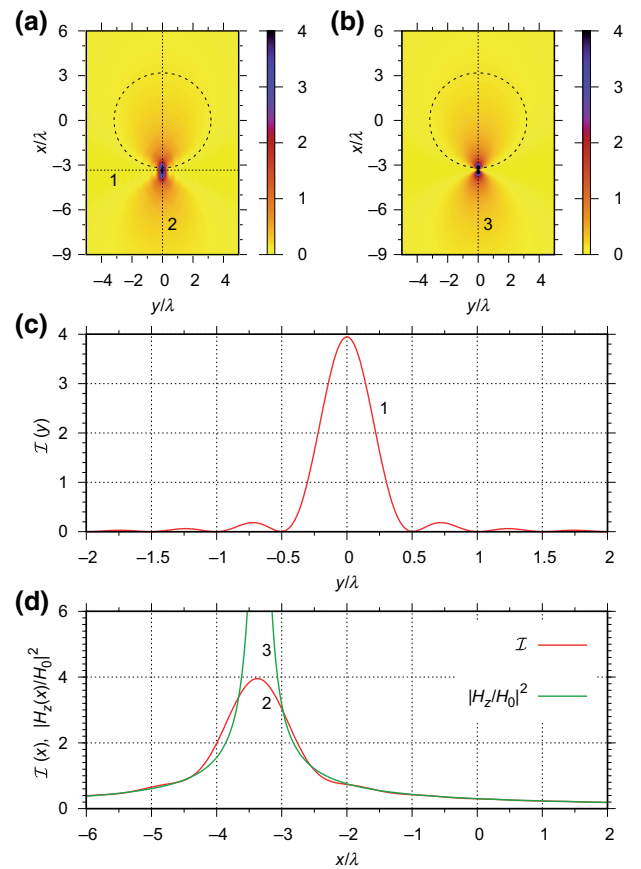


FIG. 7. The imaging of a point source located at $kd = 1$ from a particle with $kR = 20$ and a very small ($n_s = 1.005$) refractive index contrast. (a) The image as a function of the plane-of-focus position x and the transverse coordinate y . (b) The field intensity $|H_z(x, y)/H_0|^2$. (c) The image along line (1), passing through its maximum. (d) The image along vertical line (2) and the intensity along line (3). The dashed circles in panels (a) and (b) show the particle. In panel (b), the intensity range is limited by $|H_z/H_0|^2 = 4$.

We now can turn to the PSF in the presence of a particle with $n_s = 1.4$. Figure 8 shows the image intensity (i.e., PSF) and field intensity produced by a point source located at $kd = 1$ from the particle surface. The field intensity diverges at the source location, similar to the case without the particle. In the resonant case $kR = 20.382$, one can see a very efficient excitation of the WGM with $m = 24$. The images look drastically different from the intensities. For all sizes kR , an image significantly below the particle (virtual image) can be observed. The distance from the image to the particle surface increases with increasing particle size. In the resonant case, strong peaks can also be observed just below the particle.

To evaluate the resolution quantitatively, it is convenient to make cuts through the PSFs in Fig. 8. Figure 9(a) shows the image intensity at $y = 0$ as one moves along x . As the particle size kR increases, the maximum

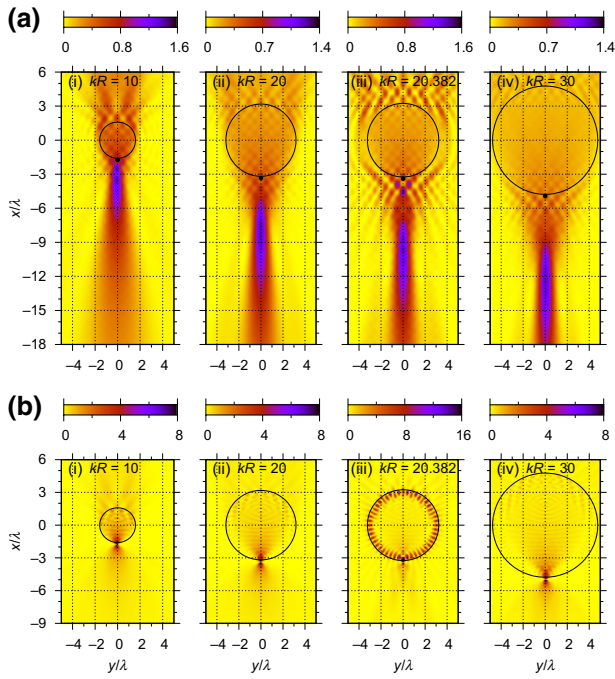


FIG. 8. The image intensity (top panels) and the field intensity (bottom panels) for a point source at $kd = 1$ below the particle. The black circles show the particles and the black dots in the top panels show the actual position of the point source.

moves from the particle boundary. There is an additional peak near the boundary in the resonant $kR = 20.382$ case. Figures 9(b1)–(b4) show the images for several plane-of-focus positions x (see also Table III). Without resonances, the narrowest peak is obtained for the smallest particle $kR = 10$ at $x/\lambda = -2.49$. For a fixed kR , the image width increases and the peak decreases as we move the plane of focus away from the particle. In the resonant case, $kR = 20.382$, one can observe significant oscillations of the PSF. The central peak has $\mathcal{W}/\lambda \approx 0.478$, which is comparable to the PSF width without the particle.

Changing the source-to-particle distance d also changes the PSF. For smaller distances, $kd < 1$, the excitation of the WGM will be even more pronounced, while nonresonant images do not change significantly. A case with larger kd , $kd = 3$, is shown in Fig. 10. For the smallest particle, $kR = 10$, the image can be obtained only if the plane of focus is at $x/\lambda = -2.481$ which is near the object plane. For the larger $kR = 20$ particle, there is also a well-defined peak just below the particle, at $x/\lambda = -4.436$. The presence of this peak can be attributed to interference effects. For $kR = 20.382$, the resonant effects become less pronounced due to rather weak coupling of the emitter to the WGM. Figure 11 shows the image intensities when the plane of focus passes through the narrow peaks for $kR = 10$ and $kR = 20$. In both cases, we obtain the width of the central peak $\mathcal{W}/\lambda = 0.6$, with significant side lobes.

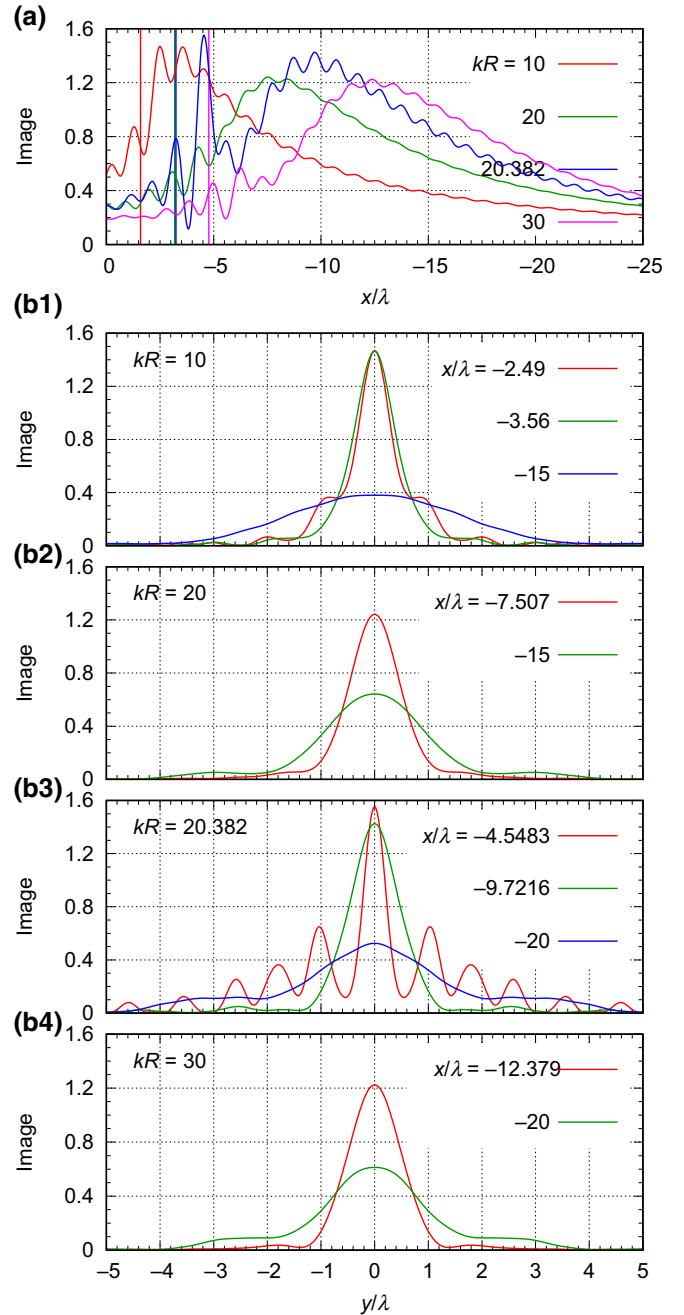


FIG. 9. Cuts through the images in Fig. 8. (a) The image intensity along x . The vertical lines indicate the particle boundary. (b1)–(b4) The image intensities along y for several plane-of-focus distances x/λ .

Figure 12 shows images in a strongly resonant case for $kR = 28.0675$ when the source is very close to the surface $kd = 0.5$. When the plane of focus is close to the particle, multiple side lobes make it difficult to relate the image to the source. It is only when the plane of focus moves significantly below the particle, at $x/\lambda = -13.9$, that reasonable but rather broad images can be obtained.

TABLE III. The properties of the images shown in Fig. 9 at various sizes kR and plane-of-focus positions x for $kd = 1$. \mathcal{W} is the width of the image and M is the magnification.

	kR	$-x/\lambda$	\mathcal{W}/λ	M	$\mathcal{W}/(M\lambda)$
1	10	2.49	0.725	1.42	0.51
2	10	3.56	0.893	2.03	0.44
3	10	15	3.68	8.57	0.43
4	20	7.507	1.07	2.25	0.48
5	20	15	2.04	4.49	0.45
6	20.382	4.5483	0.478	1.34	0.36
7	20.382	9.7216	1.06	2.86	0.37
8	20.382	20	2.3	5.88	0.41
9	30	12.379	1.15	2.51	0.46
10	30	20	1.9	4.05	0.48

The resolution is defined as the minimal distance between two points that allows them to be resolved [44, 45]. However, the microsphere provides an intrinsic magnification of the virtual image, which means that the images shown in Figs. 9 and 11 are not yet sufficient to obtain the resolution. This is because the displacement of the point source is not equal to the displacement of its image due to magnification [see Fig. 2(b)]. Using the definition of magnification M as the ratio of the image displacement and source displacement, we obtain M from the geometry:

$$M = \frac{|x|}{R + d}, \quad (11)$$

where x is the plane-of-focus position. Since, typically, $|x| > R + d$, we obtain $M > 1$. The resolution will therefore be \mathcal{W}/M , where \mathcal{W} is the FWHM of the image. Equation (11) is approximate since it does not account for various image distortions for off-axial point locations. To check its validity, the images of displaced point sources polarized along $\hat{\phi}$ are calculated. The displacements give rise to asymmetry in the images. This introduces some ambiguity into the image position, especially

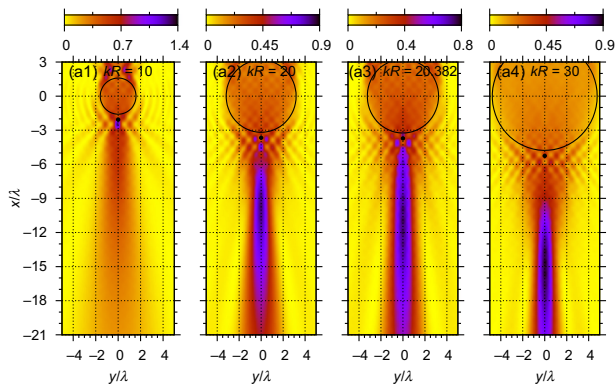


FIG. 10. Images as in Fig. 8 (top panels) but for $kd = 3$.

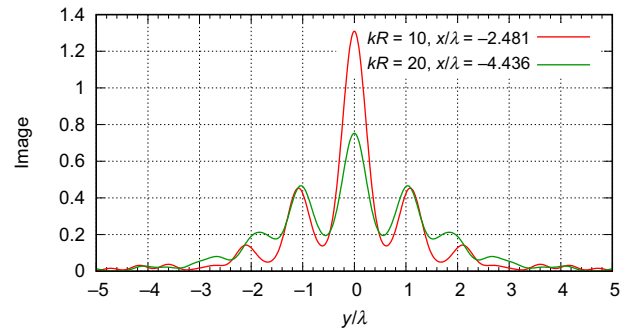


FIG. 11. Cuts through the images for $kR = 10$ and $kR = 20$ in Fig. 10.

for displacements smaller than, or comparable to, the width of the peak. Two approaches to determining the image positions are used. In the first approach, the maximum of the image peak is calculated. In the second approach, the average of two values at half maximum is calculated.

The dependencies of the magnification on the point displacement along y at a fixed plane of focus $x/\lambda = -7.5$ and several positions d of the object plane are shown in Fig. 13. In general, in all approaches moving the source from the particle, i.e., increasing kd , at the fixed plane of focus x decrease M , in agreement with Eq. (11). However, the y dependence of M varies slightly, within approximately 10%, between the approaches. The largest variations are obtained when M is calculated using the position of the maximum. Use of the middle point at half maximum gives rather good agreement with Eq. (11).

Using the images shown Fig. 9, we can calculate the resulting resolution (see Table III). The highest resolution 0.36λ is obtained in the resonant case. In all nonresonant

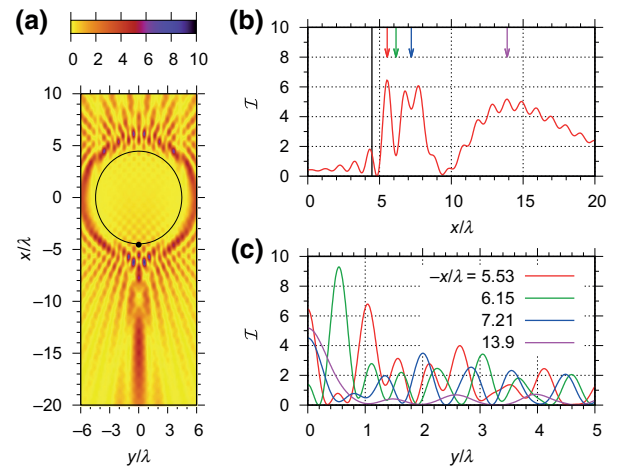


FIG. 12. Imaging in the resonant case $kR = 28.0675$, $kd = 0.5$. (a) The image intensity. (b) The image along x for $y = 0$. (c) The image along y at several values of x .

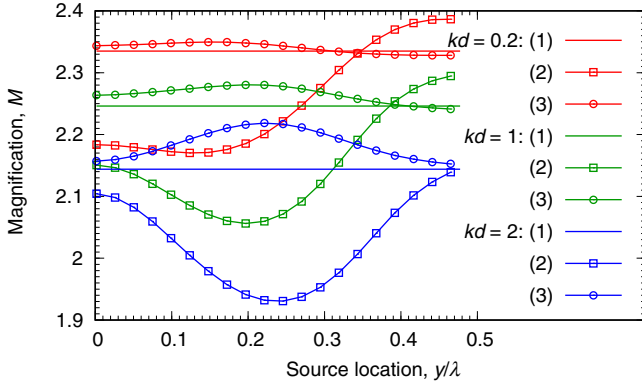


FIG. 13. The image magnification as a function of the transverse displacement y in the plane separated from the particle by distance d . The curves are obtained by three approaches: (1) using Eq. (11), (2) using the position of the image maximum, and (3) using the midpoint of the image at half maximum.

cases, the resolution is $0.4\text{--}0.5\lambda$. Note that the resolution for the smallest particle, $kR = 10$, does not show any significant improvement compared to the larger particles.

Since the PSF width \mathcal{W} and magnification M depend strongly on the plane of focus, it is instructive to find the highest resolution achievable for various point-source locations kd by moving along x . The results are summarized in Fig. 14. For comparison with the photonic nanojet widths, we note that for the sufficiently large microspheres selected for this analysis, the nanojet nonresonant ($kR = 20$) width (0.49λ) is very close to the diffraction limit (0.5λ) indicated in Fig. 14, whereas the nanojet resonant ($kR = 20.382$) width (0.39λ) is smaller than the diffraction limit.

The highest resolution is typically around $0.4\text{--}0.5\lambda$. In the resonant case, the resolution can exceed these values slightly and reach approximately 0.3λ for sources very close to the particle surface. This means that for high-index microspheres ($n_s \sim 2$) immersed in liquids or

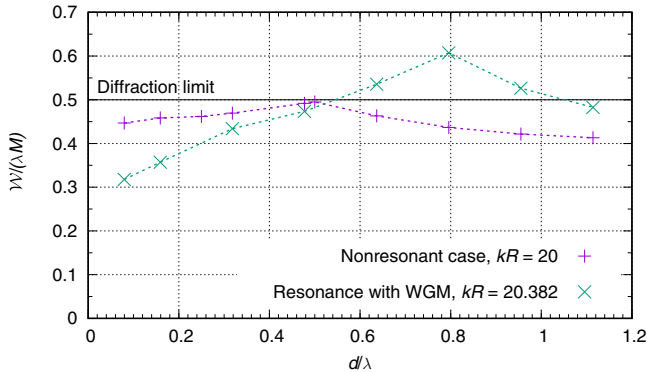


FIG. 14. The resolution $\mathcal{W}/(\lambda M)$ for various locations of the point source d/λ for $kR = 20$ and $kR = 20.382$.

embedded in elastomeric slabs, with $n_b \sim 1.4$, the resolution values can reach about 0.2λ . However, in this case, noticeable side lobes can be obtained on the images. Another interesting observation is that in the nonresonant case, the maximal resolution, about 0.4λ , can be achieved for point sources separated from the microsphere by a λ -scale distance. Here again, the increase in the resolution is accompanied by the appearance of side lobes (see Fig. 11). The resolution becomes markedly better than the width of a photonic nanojet (0.49λ) [see Fig. 6(b)].

VIII. COMPARISON OF PHOTONIC NANOJETS AND PSF PROPERTIES

Using the results from the previous sections, we can now compare the relevance of nanojet properties to the resolution, which is defined by the PSF and magnification. It is important to realize that the nanojet properties depend only on two parameters: the size parameters kR and the refractive index n_s . The most relevant nanojet characteristics are the location of the nanojet maximum and the transverse width. The PSF can also be characterized by the plane-of-focus positions, at which the image intensity is at a maximum, and the corresponding image width. The plane-of-focus position determines the magnification. The PSF also depends on the gap d , which greatly affects imaging [10,11]. Thus, the imaging regime involves more parameters compared to the focusing regime.

Let us consider the nonresonant case in detail. Small particles with $kR = 10$ produce nanojets at the particle surface, with the smallest width of 0.32λ . Larger particles, with $kR \sim 20\text{--}30$, produce nanojets that are well separated, by approximately λ , from the surface and have a larger width, of approximately $0.5\text{--}0.6\lambda$. Note that the nanojet width is significantly smaller for $kR = 10$ as compared to $kR = 20$ or $kR = 30$. The widths of the PSFs (see Figs. 8 and 9 and Table III) at the maxima, which are well separated from the particle surface, increase from $\mathcal{W}/\lambda = 0.725$ for $kR = 10$ to $\mathcal{W}/\lambda = 1.15$ for $kR = 30$. Thus, the PSF width is significantly larger than the nanojet width. Accounting for magnification allows finding the true resolution. The resolution changes slightly from 0.51 to 0.46 as the size increases from $kR = 10$ to $kR = 30$. Moving the plane of focus further away for the $kR = 10$ particle increases its resolution up to 0.43 , which is slightly better than 0.46 for the $kR = 30$ particle. While the nanojet width decreases significantly as the particle becomes smaller, there is no significant enhancement of the resolution. This allows one to conclude that the actual values of the nanojet width and the PSF-based resolution differ and do not show the expected correlation.

To extend the search for a possible correlation, let us try to compare the nanojet width and resolution in several related cases. In the first case, we calculate the field intensity produced by a plane wave and find the location at

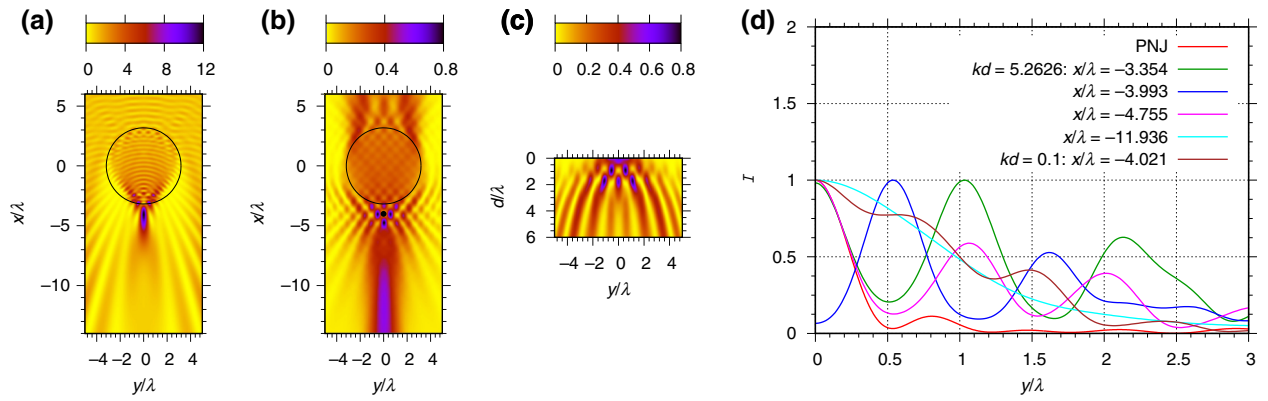


FIG. 15. (a) The field intensity $|H_z(x,y)|^2$ produced by a plane wave incident on a particle with $kR = 20$. The nanojet created has a maximum at $kx = -25.2626$ ($x/\lambda = -4.020$). (b) The image produced by a point source located at the position of the nanojet maximum $kd = 5.2626$. (c) The image observed at the plane of focus $kx = -25.2626$ for various positions of the point source kd . (d) Cuts of the distributions shown in (a)–(c). All curves in (d) are normalized to their maxima.

which the created nanojet has its maximum. In the second case, we put a point source at this location and calculate its image for various plane-of-focus positions. In the third case, we fix the plane of focus at the nanojet maximum and vary the point-source location.

The results of the three cases are shown in Fig. 15. The location of the nanojet maximum is relatively far from the particle, at $d/\lambda = 0.84$, and its FWHM is 0.5λ [see Fig. 15(a)]. Thus, putting a point source at this location results in various interference effects (significant side lobes and even the lack of a central peak) when the plane of focus is near the particle [see Fig. 15(b) and the curves for $x/\lambda = -3.354$, $x/\lambda = -3.993$ in Fig. 15(c)]. When the plane of focus is further away from the particle, at $x/\lambda = -4.755$ and $x/\lambda = -11.936$, the side lobes become smaller and the central peak becomes wider. In order to find the resolution, we need to account for magnification for $kd = 5.2626$: $M = 0.83$ at $x/\lambda = -3.354$; $M = 0.99$ at $x/\lambda = -3.993$; $M = 1.2$ at $x/\lambda = -4.755$; and $M = 3.0$ at $x/\lambda = -11.936$. The best resolution, 0.42λ , is for $x/\lambda = -4.755$. If we fix the plane of focus [Fig. 15(a)], the only possibility for obtaining an image is to put the object right next to the particle [see Fig. 15(c)] but in this case the image is rather broad, with a resolution of approximately 1.6λ . Overall, comparing the nanojet width, 0.5λ , and the achievable resolution, we obtain that, depending on the observation conditions, the resolution varies significantly. The highest resolution is 0.42λ but the PSF has significant side lobes. Again, the nanojet width and the resolution are rather different.

IX. CONCLUSION

To conclude, the resolution of microsphere-based nanoscopy has historically been studied using two different approaches. In the first approach, the resolution

was associated with the width of the photonic nanojets, the justification being rooted in the reciprocity principle [1,28,33–43]. In the second, more direct, approach, the resolution was defined as the FWHM of the PSF [21–26]. This situation created an ambiguity, since no specific relation between the results of the two approaches was established. In addition, rigorous experimental quantification of the resolution, typically performed with imaging nanoplasmonic structures, led to resolution values (approximately $\lambda/7$ [8,10–12,18]) that are higher than the resolution estimations obtained by either of these theoretical approaches.

We rigorously compare the results of the resolution-quantification techniques by solving the Maxwell equations for focusing and for point-source emission. The calculated PSF accounts for all transformation of the evanescent near fields to the propagating field that can take place for deeply subwavelength source-to-microsphere gaps. The analysis is performed for refractive indexes of $n_s = 1.4$ for the particle and $n_b = 1$ for the background, for various particle sizes ($10 < kR < 30$ or $3.2 < D/\lambda < 9.5$) and particle-to-source distances $0 < d/\lambda \lesssim 1$. We show that the reciprocity principle applied to focusing does not provide accurate information about the resolution in microspherical imaging.

Two imaging regimes, resonant and nonresonant, are studied. The resonant imaging can be realized even for broadband excitation due to the strong coupling of point emission to WGMs. In the nonresonant regime and for deeply subwavelength gaps, $d \lesssim 0.15\lambda$, the virtual images are formed at distances of about D below the particle, which significantly exceeds the wavelength. The resultant depth of field is also much larger than the wavelength. The image has rather high magnification and the resolution can reach $0.4–0.5\lambda$. In the resonant regime, virtual images can also be observed at distances of about λ below the particles

and with a smaller magnification. The resolution can reach 0.35λ but the images suffer from side lobes. Moreover, the use of very high- Q resonances makes imaging practically impossible due to multiple side lobes.

Sources separated from the microspheres by distances of about λ can also produce images. One can obtain the usual virtual images for rather large particles. In addition, for small particles there are images at distances at about $1-1.5\lambda$. The resolution of such separated sources can reach $0.4-0.5\lambda$.

In general, the obtained resolution in the nonresonant cases is comparable to (but slightly worse than) the SIL limit in a material with a refractive index equal to that of the microsphere, that is, $\lambda/(2n_s) = 0.36\lambda$. The resolution in the presence of a background with $n_b > 1$ will be higher by the same value n_b as long as n_s increases proportionally. This means that our results are applicable to a wide range of situations in which high-index ($n_s \sim 2$) microspheres are fully liquid immersed [6–8] or embedded in elastomeric slabs [10–12]. Accounting for the background index means that the resonant resolution can be about 0.2λ , while the nonresonant resolution can be about 0.3λ . Both resolution values are worse than the experimentally measured ones.

We find that there is no significant quantitative correlation between the nanojet width and the resolution predicted from the PSF. While there are certainly similarities between focusing and imaging, they also have considerable differences, which make the use of nanojet properties rather weakly relevant to imaging.

There is another effect related to photonic nanojets—the possibility of strongly enhancing the backscattering of a nanoparticle by placing it in the photonic-nanojet region of a microsphere. As shown in Ref. [67], the enhancement comes from the field focusing by the microsphere and from the multiple scattering between the nanoparticle and the microsphere. While the enhanced backscattering may affect imaging to some extent, it is not likely to play a role in the experimental superresolution. Indeed, in the imaging experiments, the objects are separated from the microspheres by distances much smaller than the wavelength. In contrast, photonic nanojets reach a maximum at distances comparable to the wavelength, unless the particle is small (see Fig. 6). The substrate can also prevent nanojet formation. In addition, the enhanced backscattering is not likely to explain the superresolution either. Indeed, the illumination of a system consisting of a microsphere and a nanoparticle (the imaged object) leads to the excitation of optical polarization in the nanoparticle, which can be calculated. After that, the nanoparticle can be modeled as a polarization (or current) source without affecting the field distribution outside of it. Due to the smallness of the nanoparticle, the source can be approximated by the delta function with the calculated amplitude. Moreover, the image is produced only by the fields emitted by this current, so the fields created directly by the

external illumination can be left out when calculating the virtual images. This leaves us with the exact problem considered here—the emission of a pointlike current. The polarizability of the nanoparticle and its interaction with the microsphere determines the source amplitude, which affects the image contrast but not the PSF width.

In Ref. [24], the superresolution of microspheres was attributed to the mechanism of scanning near-field optical microscopy (SNOM), in which the microsphere acts as a tip, enabling the conversion of evanescent waves to propagating waves. Such transformations are fully accounted for in our approach. Indeed, while we use cylindrical waves, the radiation of the point source can also be expanded into propagating and evanescent plane waves incident on the microsphere. However, no superresolution is obtained. Apparently, such conversion is rather weak due to the large size of the microspheres. In addition, in some situations the microspheres were partly immersed in a liquid such as ethanol with $n_b = 1.36$ [18,68]. In such cases the refractive index contrast with silica microspheres ($n_s = 1.36$) at their bottom section exposed to the liquid is rather small to expect significant refraction and conversion of evanescent-to-propagating waves at this interface.

Thus, while the classical PSF is considered to be the key characteristic in microscopy, it does not explain the superresolution observed in the microspherical experiments. It is a very compelling situation since theoretical estimations, especially using ideal systems, commonly overestimate experimental results. Microspherical imaging certainly involves some physical mechanism that are not accounted for here. For example, coherent effects [25,60,64] can be especially pronounced in the presence of localized plasmons [16,57,58] and WGMs.

More generally, it should be noted that the role of plasmonics in achieving superresolution imaging through microspheres can be quite dramatic. This role can be revealed via two different mechanisms. The first is related to localized plasmonic structured illumination microscopy (LPSIM) [29,59], which stems from the ideas of regular structured illumination microscopy (SIM) [69,70]. In this approach, coupling with the periodic nanoplasmonic array located just below the object leads to a preservation of the information about the subdiffraction features of the object, due to the folding of the photonic dispersions into the escape cone. Such information presents in the form of Moiré fringes and the reconstruction of the super resolved image requires postimaging processing. The second mechanism becomes possible in the case of using nanoplasmonic arrays with extremely short periods (< 100 nm), which make coupling to the band structure impossible [58]. In the latter case, fluorescent objects can be locally coupled to “hot spots” in the underlying plasmonic metasurface due to localized surface-plasmon resonances in the adjacent metallic nanodisks of the arrays. In the case of sufficiently small gaps

(< 20 nm) between the nanodisks, the hot spots can be localized in the gaps separating them [71,72]. The emission mediated by coupling with such plasmonic hot spots contains modes with very large in-plane k vectors, which can be near-field coupled into the high-index microspheres placed in contact with such objects and can contribute to the formation of their virtual images. In contrast to a regular LPSIM, the latter mechanism does not require any postimaging processing. Superresolution according to the second mechanism has been proposed [57] and realized [16,58] for the imaging of dye-doped nanospheres and F -actin proteins. The use of nanoplasmonic arrays, as well as the use of coherent or partly coherent illumination, especially at oblique incidence, requires further theoretical investigation and these factors can significantly increase the experimental resolution of microspherical nanoscopy.

ACKNOWLEDGMENTS

The authors would like to thank Aaron Brettin for help with preparation of Fig. 1(a).

- [1] Z. Wang, W. Guo, L. Li, B. Lukyanchuk, A. Khan, Z. Liu, Z. Chen, and M. Hong, Optical virtual imaging at 50 nm lateral resolution with a white-light nanoscope, *Nat. Commun.* **2**, 218 (2011).
- [2] S. M. Mansfield and G. S. Kino, Solid immersion microscope, *Appl. Phys. Lett.* **57**, 2615 (1990).
- [3] B. D. Terris, H. J. Mamin, D. Rugar, W. R. Studenmund, and G. S. Kino, Near field optical data storage using a solid immersion lens, *Appl. Phys. Lett.* **65**, 388 (1994).
- [4] Y. Gambin, O. Legrand, and S. R. Quake, Microfabricated rubber microscope using soft solid immersion lenses, *Appl. Phys. Lett.* **88**, 174102 (2006).
- [5] V. N. Astratov and A. Darafsheh, Methods and systems for superresolution optical imaging using high-index of refraction microspheres and microcylinders, U.S. patent application 14/042,834 (2013); U.S. provisional application 61/656,710 (7 June 2012), <https://www.google.com/patents/US20140355108>.
- [6] A. Darafsheh, G. F. Walsh, L. Dal Negro, and V. N. Astratov, Optical super-resolution by high-index liquid-immersed microspheres, *Appl. Phys. Lett.* **101**, 141128 (2012).
- [7] A. Darafsheh, N. I. Limberopoulos, J. S. Derov, D. E. Walker, Jr., and V. N. Astratov, Advantages of microsphere-assisted super-resolution imaging technique over solid immersion lens and confocal microscopies, *Appl. Phys. Lett.* **104**, 061117 (2014).
- [8] K. W. Allen, N. Farahi, Y. C. Li, N. I. Limberopoulos, D. E. Walker, A. M. Urbas, and V. N. Astratov, Overcoming the diffraction limit of imaging nanoplasmonic arrays by microspheres and microfibers, *Opt. Express* **23**, 24484 (2015).
- [9] K. W. Allen, N. Farahi, Y. Li, N. I. Limberopoulos, D. E. Walker, Jr., A. M. Urbas, and V. N. Astratov, in *NAECON 2014—IEEE National Aerospace and Electronics Conference* (IEEE, Dayton, OH, 2014), p. 50.
- [10] K. W. Allen, N. Farahi, Y. C. Li, N. I. Limberopoulos, D. E. Walker, A. M. Urbas, V. Liberman, and V. N. Astratov, Super-resolution microscopy by movable thin-films with embedded microspheres: Resolution analysis, *Ann. Phys.* **527**, 513 (2015).
- [11] K. W. Allen, Y. Li, and V. N. Astratov, Reply to “Comment on ‘Super-resolution microscopy by movable thin-films with embedded microspheres: Resolution analysis’ [Ann. Phys. (Berlin) 527, 513 (2015)]”, *Ann. Phys.* **528**, 901 (2016).
- [12] V. N. Astratov, K. W. Allen, N. Farahi, Y. Li, N. I. Limberopoulos, D. E. Walker, Jr., A. M. Urbas, V. Liberman, and M. Rothschild, Optical nanoscopy with contact microlenses overcomes the diffraction limit, SPIE Newsroom, February 11 (2016).
- [13] L. Li, W. Guo, Y. Yan, S. Lee, and T. Wang, Label-free super-resolution imaging of adenoviruses by submerged microsphere optical nanoscopy, *Light: Sci. Appl.* **2**, e104 (2013).
- [14] H. Yang, N. Moullan, J. Auwerx, and M. A. M. Gijs, Super-resolution biological microscopy using virtual imaging by a microsphere nanoscope, *Small* **10**, 1712 (2014).
- [15] A. Brettin, K. F. Blanchette, Y. Nesmelov, N. I. Limberopoulos, A. M. Urbas, and V. N. Astratov, in *NAECON 2016—IEEE National Aerospace and Electronics Conference (NAECON) and Ohio Innovation Summit (OIS)* (IEEE, Dayton, OH, 2016), p. 269.
- [16] V. N. Astratov, A. V. Maslov, A. Brettin, K. F. Blanchette, Y. E. Nesmelov, N. I. Limberopoulos, D. E. Walker, and A. M. Urbas, Contact microspherical nanoscopy: From fundamentals to biomedical applications, *Proc. SPIE* **10077**, 100770S (2017).
- [17] L. A. Krivitsky, J. J. Wang, Z. Wang, and B. Luk'yanchuk, Locomotion of microspheres for super-resolution imaging, *Sci. Rep.* **3**, 3501 (2013).
- [18] F. Wang, L. Liu, H. Yu, Y. Wen, P. Yu, Z. Liu, Y. Wang, and W. J. Li, Scanning superlens microscopy for non-invasive large field-of-view visible light nanoscale imaging, *Nat. Commun.* **7**, 13748 (2016).
- [19] J. Li, W. Liu, T. Li, I. Rozen, J. Zhao, B. Bahari, B. Kante, and J. Wang, Swimming microrobot optical nanoscopy, *Nano Lett.* **16**, 6604 (2016).
- [20] M. Duocastella, F. Tantussi, A. Haddadpour, R. P. Zaccaria, A. Jacassi, G. Veronis, A. Diaspro, and F. De Angelis, Combination of scanning probe technology with photonic nanojets, *Sci. Rep.* **7**, 3474 (2017).
- [21] Y. Duan, G. Barbastathis, and B. Zhang, Classical imaging theory of a microlens with super-resolution, *Opt. Lett.* **38**, 2988 (2013).
- [22] V. M. Sundaram and S.-B. Wen, Analysis of deep sub-micron resolution in microsphere based imaging, *Appl. Phys. Lett.* **105**, 204102 (2014).
- [23] T. X. Hoang, Y. Duan, X. Chen, and G. Barbastathis, Focusing and imaging in microsphere-based microscopy, *Opt. Express* **23**, 12337 (2015).
- [24] Y. Ben-Aryeh, Increase of resolution by use of microspheres related to complex Snell's law, *J. Opt. Soc. Am. A* **33**, 2284 (2016).
- [25] A. V. Maslov and V. N. Astratov, Imaging of sub-wavelength structures radiating coherently near microspheres, *Appl. Phys. Lett.* **108**, 051104 (2016).

- [26] A. V. Maslov and V. N. Astratov, Optical nanoscopy with contact Mie-particles: Resolution analysis, *Appl. Phys. Lett.* **110**, 261107 (2017).
- [27] Y. Yan, L. Li, C. Feng, W. Guo, S. Lee, and M. Hong, Microsphere-coupled scanning laser confocal nanoscope for sub-diffraction-limited imaging at 25 nm lateral resolution in the visible spectrum, *ACS Nano* **8**, 1809 (2014).
- [28] H. Yang, R. Trouillon, G. Huszka, and M. A. M. Gijs, Super-resolution imaging of a dielectric microsphere is governed by the waist of its photonic nanojet, *Nano Lett.* **16**, 4862 (2016).
- [29] A. Bezryadina, J. Li, J. Zhao, A. Kothambawala, J. Ponsetto, E. Huang, J. Wang, and Z. Liu, Localized plasmonic structured illumination microscopy with an optically trapped microlens, *Nanoscale* **9**, 14907 (2017).
- [30] G. Huszka, H. Yang, and M. A. M. Gijs, Microsphere-based super-resolution scanning optical microscope, *Opt. Express* **25**, 15079 (2017).
- [31] R. J. Potton, Reciprocity in optics, *Rep. Prog. Phys.* **67**, 717 (2004).
- [32] A. Maznev, A. Every, and O. Wright, Reciprocity in reflection and transmission: What is a phonon diode? *Wave Motion* **50**, 776 (2013).
- [33] B. Du, Y.-H. Ye, J. Hou, M. Guo, and T. Wang, Sub-wavelength image stitching with removable microsphere-embedded thin film, *Appl. Phys. A* **122**, 15 (2016).
- [34] M. Guo, Y.-H. Ye, J. Hou, and B. Du, Size-dependent optical imaging properties of high-index immersed microsphere lens, *Appl. Phys. B* **122**, 65 (2016).
- [35] C. A. González Mora, M. Hartelt, D. Bayer, M. Aeschlimann, E. A. Ilin, and E. Oesterschulze, Microsphere-based cantilevers for polarization resolved and femtosecond SNOM, *Appl. Phys. B* **122**, 86 (2016).
- [36] H. S. S. Lai, F. Wang, Y. Li, B. Jia, L. Liu, and W. J. Li, Super-resolution real imaging in microsphere-assisted microscopy, *PLoS ONE* **11**, e0165194 (2016).
- [37] G. Gu, R. Zhou, H. Xu, G. Cai, and Z. Cai, Subsurface nano-imaging with self-assembled spherical cap optical nanoscopy, *Opt. Express* **24**, 4937 (2016).
- [38] M. Guo, Y.-H. Ye, J. Hou, B. Du, and T. Wang, Imaging of sub-surface nanostructures by dielectric planer cavity coupled microsphere lens, *Optics Commun.* **383**, 153 (2017).
- [39] I. Kassamakov, S. Lecler, A. Nolvi, A. Leong-Hoi, P. Montgomery, and E. Hæggröm, 3D super-resolution optical profiling using microsphere enhanced Mirau interferometry, *Sci. Rep.* **7**, 3683 (2017).
- [40] J. Ling, X. Wang, D. Li, and X. Liu, Modelling and verification of white light oil immersion microsphere optical nanoscope, *Opt. Quant. Electron.* **49**, 377 (2017).
- [41] S. Yang, F. Wang, Y.-H. Ye, Y. Xia, Y. Deng, J. Wang, and Y. Cao, Influence of the photonic nanojet of microspheres on microsphere imaging, *Opt. Express* **25**, 27551 (2017).
- [42] Y. Zhou, Y. Tang, Q. Deng, L. Zhao, and S. Hu, Contrast enhancement of microsphere-assisted super-resolution imaging in dark-field microscopy, *Appl. Phys. Express* **10**, 082501 (2017).
- [43] F. Wang, S. Yang, H. Ma, P. Shen, N. Wei, M. Wang, Y. Xia, Y. Deng, and Y.-H. Ye, Microsphere-assisted super-resolution imaging with enlarged numerical aperture by semi-immersion, *Appl. Phys. Lett.* **112**, 023101 (2018).
- [44] J. W. Goodman, *Introduction to Fourier Optics* (The McGraw-Hill Companies, 1996), 2nd ed.
- [45] A. J. den Dekker and A. van den Bos, Resolution: A survey, *J. Opt. Soc. Am. A* **13**, 547 (1997).
- [46] Z. Chen, A. Taflove, and V. Backman, Photonic nanojet enhancement of backscattering of light by nanoparticles: A potential novel visible-light ultramicroscopy technique, *Opt. Express* **12**, 1214 (2004).
- [47] X. Li, Z. Chen, A. Taflove, and V. Backman, Optical analysis of nanoparticles via enhanced backscattering facilitated by 3-D photonic nanojets, *Opt. Express* **13**, 526 (2005).
- [48] M.-S. Kim, T. Scharf, S. Mühlig, C. Rockstuhl, and H. P. Herzig, Engineering photonic nanojets, *Opt. Express* **19**, 10206 (2011).
- [49] B. S. Luk'yanchuk, R. Paniagua-Domínguez, I. Minin, O. Minin, and Z. Wang, Refractive index less than two: Photonic nanojets yesterday, today and tomorrow [Invited], *Opt. Mater. Express* **7**, 1820 (2017).
- [50] Y. E. Geints, Z. A. Zemlyanov, and E. K. Panina, Photonic jets from resonantly excited transparent dielectric microspheres, *J. Opt. Soc. Am. B* **29**, 758 (2012).
- [51] M. Mansuripur, Reversibility in classical linear optics, *Opt. Photonics News* **9**, 53 (1998).
- [52] P. K. Upputuri and M. Pramanik, Microsphere-aided optical microscopy and its applications for super-resolution imaging, *Optics Commun.* **404**, 32 (2017).
- [53] A. Heifetz, S.-C. Kong, A. V. Sahakian, A. Taflove, and V. Backman, Photonic nanojets, *J. Comput. Theor. Nanosci.* **6**, 1979 (2009).
- [54] X. Hao, X. Liu, C. Kuang, Y. Li, Y. Ku, H. Zhang, H. Li, and L. Tong, Far-field super-resolution imaging using near-field illumination by micro-fiber, *Appl. Phys. Lett.* **102**, 013104 (2013).
- [55] I. R. Capoglu, A. Taflove, and V. Backman, Angora: A free software package for finite-difference time-domain electromagnetic simulation, *IEEE Antennas Propag. Mag.* **55**, 80 (2013).
- [56] A. V. Boriskina, S. V. Boriskina, A. Rolland, R. Sauleau, and A. I. Nosich, Test of the FDTD accuracy in the analysis of the scattering resonances associated with high- Q whispering-gallery modes of a circular cylinder, *J. Opt. Soc. Am. A* **25**, 1169 (2008).
- [57] V. N. Astratov, N. I. Limberopoulos, and A. Urbas, Super-resolution microscopy methods and systems enhanced by dielectric microspheres or microcylinders used in combination with metallic nanostructures, U.S. patent 983,587,0B2 (5 June 2015). <https://patents.google.com/patent/US9835870B2/en>.
- [58] A. Brettin, F. Abolmaali, K. F. Blanchette, C. L. McGinnis, Y. E. Nesmelov, N. I. Limberopoulos, D. E. Walker, Jr., I. Anisimov, A. M. Urbas, L. Poffo, A. V. Maslov, and V. N. Astratov, Enhancement of resolution in microspherical nanoscopy by coupling of fluorescent objects to plasmonic metasurface, *Appl. Phys. Lett.* **114**, 131101 (2019).
- [59] J. L. Ponsetto, A. Bezryadina, F. Wei, K. Onishi, H. Shen, E. Huang, L. Ferrari, Q. Ma, Y. Zou, and Z. Liu, Experimental demonstration of localized plasmonic structured illumination microscopy, *ACS Nano* **11**, 5344 (2017).

- [60] P. von Olshausen and A. Rohrbach, Coherent total internal reflection dark-field microscopy: Label-free imaging beyond the diffraction limit, *Opt. Lett.* **38**, 4066 (2013).
- [61] A. V. Maslov and V. N. Astratov, Microspherical photonics: Sorting resonant photonic atoms by using light, *Appl. Phys. Lett.* **105**, 121113 (2014).
- [62] M. V. Klibanov, N. A. Koshev, D.-L. Nguyen, L. H. Nguen, A. Brettin, and V. N. Astratov, A numerical method to solve a phaseless coefficient inverse problem from a single measurement of experimental data, *SIAM J. Imaging Sci.* **11**, 2339 (2018).
- [63] H. Guo, Y. Han, X. Weng, Y. Zhao, G. Sui, Y. Wang, and S. Zhuang, Near-field focusing of the dielectric microsphere with wavelength scale radius, *Opt. Express* **21**, 2434-2443 (2013).
- [64] S. Perrin, S. Lecler, A. Leong-Hoi, and P. C. Montgomery, Role of coherence in microsphere-assisted nanoscopy, *Proc. SPIE 10330 Model. Aspects Opt. Metrol. VI 103300V* (2017).
- [65] W. V. Houston, A compound interferometer for fine structure work, *Phys. Rev. B* **29**, 478 (1927).
- [66] Lord Rayleigh, Investigations in optics, with special reference to the spectroscope, *Philos. Mag.* **8**, 261 (1879).
- [67] Z. Chen, A. Taflove, X. Li, and V. Backman, Superenhanced backscattering of light by nanoparticles, *Opt. Lett.* **31**, 196 (2006).
- [68] X. Hao, C. Kuang, X. Liu, H. Zhang, and Y. Li, Microsphere based microscope with optical super-resolution capability, *Appl. Phys. Lett.* **99**, 203102 (2011).
- [69] M. G. L. Gustafsson, L. Shao, P. M. Carlton, C. J. R. Wang, I. N. Golubovskaya, W. Z. Cande, D. A. Agard, and J. W. Sedat, Three-dimensional resolution doubling in wide-field fluorescence microscopy by structured illumination, *Biophys. J.* **94**, 4957 (2008).
- [70] F. Ströhl, and C. F. Kaminski, Frontiers in structured illumination microscopy, *Optica* **3**, 667 (2016).
- [71] J. R. Krenn, A. Dereux, J. C. Weeber, E. Bourillot, Y. Lacroute, J. P. Goudonnet, G. Schider, W. Gotschy, A. Leitner, F. R. Aussenegg, and C. Girard, Squeezing the Optical Near-Field Zone by Plasmon Coupling of Metallic Nanoparticles, *Phys. Rev. Lett.* **92**, 2590 (1999).
- [72] N. J. Halas, S. Lal, W.-S. Chang, S. Link, and P. Nordlander, Plasmons in strongly coupled metallic nanostructures, *Chem. Rev.* **111**, 3913 (2011).